nature astronomy

Article

https://doi.org/10.1038/s41550-022-01865-y

Magnetar spin-down glitch clearing the way for FRB-like bursts and a pulsed radio episode

Received: 22 July 2022

Accepted: 14 November 2022

Published online: 12 January 2023

Check for updates

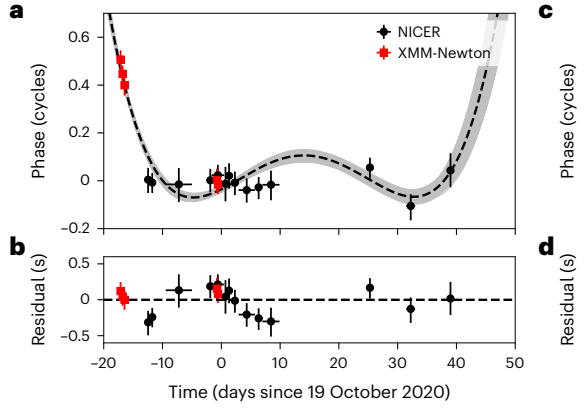
G. Younes ® ^{1,2} ⋈, M. G. Baring ® ³ ⋈, A. K. Harding ⁴, T. Enoto ⁵, Z. Wadiasingh ^{1,6,7}, A. B. Pearlman ^{8,9,10}, W. C. G. Ho ® ¹¹, S. Guillot ® ^{12,13}, Z. Arzoumanian ¹, A. Borghese ® ^{14,15}, K. Gendreau ® ¹, E. Göğüş ® ¹⁶, T. Güver ¹⁷, A. J. van der Horst ® ², C.-P. Hu ¹⁸, G. K. Jaisawal ® ¹⁹, C. Kouveliotou ², L. Lin ²⁰ & W. A. Majid ® ^{10,21}

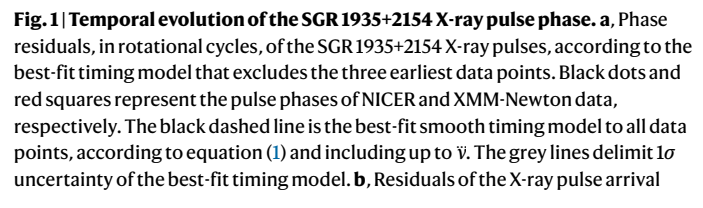
Magnetars are a special subset of the isolated neutron star family, with X-ray and radio emission mainly powered by the decay of their immense magnetic fields. Many attributes of magnetars remain poorly understood: spin-down glitches or the sudden reductions in the star's angular momentum, radio bursts reminiscent of extragalactic fast radio bursts (FRBs) and transient pulsed radio emission lasting months to years. Here we unveil the detection of a large spin-down glitch event (fractional change in spin frequency $|\Delta\nu/\nu| = 5.8^{+2.6}_{-1.6} \times 10^{-6})$ from the magnetar SGR 1935+2154 on 5 October 2020 (±1 day). We find no change to the source-persistent surface thermal or magnetospheric X-ray behaviour, nor is there evidence of strong X-ray bursting activity. Yet, in the subsequent days, the magnetar emitted three FRB-like radio bursts followed by a month-long episode of pulsed radio emission. Given the rarity of spin-down glitches and radio signals from magnetars, their approximate synchronicity suggests an association, providing pivotal clues to their origin and triggering mechanisms with ramifications to the broader magnetar and FRB populations. We postulate that impulsive crustal plasma shedding close to the magnetic pole generates a wind that combs out magnetic field lines, rapidly reducing the star's angular momentum while temporarily altering the magnetospheric field geometry to permit the pair creation needed to precipitate radio emission.

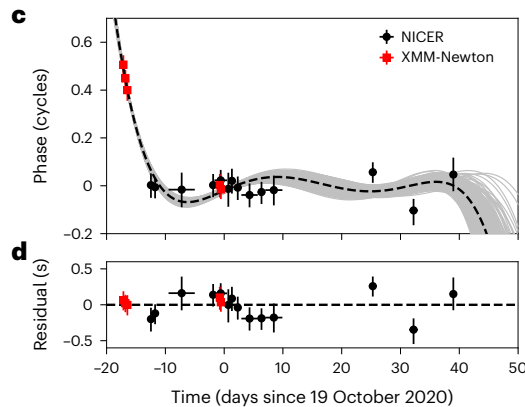
SGR1935+2154 is an isolated neutron star displaying hot and luminous soft X-ray emission pulsed 1 at a spin frequency $\nu\approx0.308$ Hz while slowing down at a nominal rate of about -1.4×10^{-12} Hz s $^{-1}$. If attributed to magnetic dipole braking, these spin properties imply a dipole magnetic field strength $B\approx2.2\times10^{14}$ G at the equator and a young spin-down age $\tau\approx3.6$ kyr. SGR 1935+2154 is also a prolific burster 2 , capable of displaying in a matter of minutes hundreds of bright millisecond-duration X-ray bursts 3 , with luminosities exceeding 1.0×10^{41} erg s $^{-1}$. Hence, SGR

1935+2154 belongs to the small, special group of isolated neutron stars known as magnetars, for which the very strong magnetic field powers their many emission characteristics. Due to their extreme, variable nature and large magnetic energy budget, magnetars are the leading suspect for the sources of enigmatic bright millisecond radio flashes of extragalactic origin known as fast radio bursts (FRBs)⁴. In a rare occurrence, on 28 April 2020, during a period of intense X-ray bursting activity³, SGR 1935+2154 emitted a radio burst with a luminosity approaching

A full list of affiliations appears at the end of the paper. Me-mail: george.a.younes@nasa.gov; baring@rice.edu







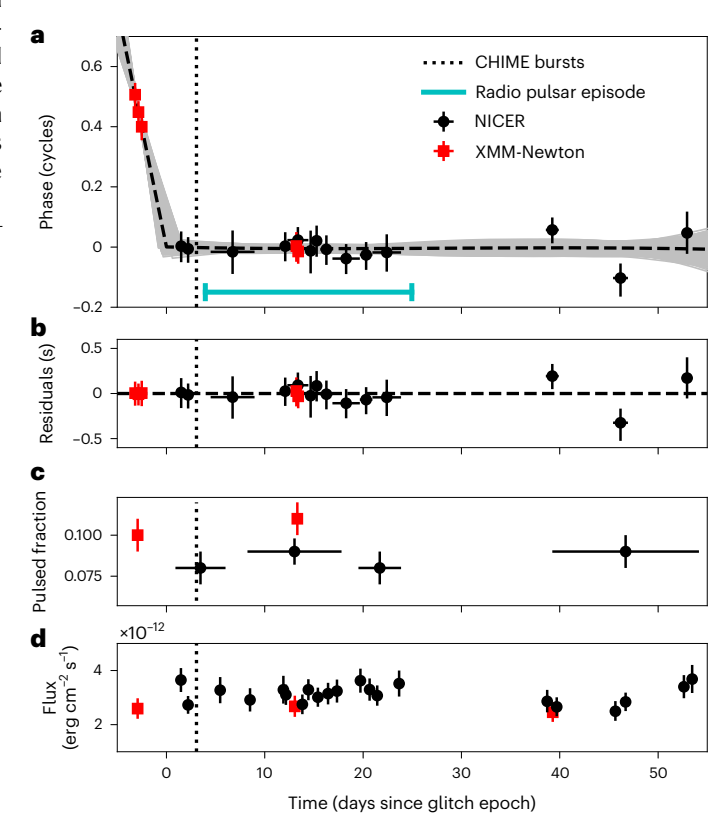
times in seconds from the latter. \mathbf{c} , Same as \mathbf{a} , except that the timing model includes up to $\ddot{\mathbf{v}}$. Note that this model has the same number of free parameters as the one shown in Fig. 2. \mathbf{d} , Residuals of the X-ray pulse arrival times in seconds from the best-fit timing model shown in \mathbf{c} . In all panels, the vertical line on each data point is the 1σ uncertainty on those measurements. In all panels, the horizontal lines on each data point indicate the temporal extent utilized to measure a pulse TOA.

extragalactic FRBs. This discovery provided the first evidence for the nature of the progenitor of at least some FRBs.^{5,6}.

Since this event, we have been monitoring SGR 1935+2154 regularly with several X-ray instruments, most notably in the soft, 1-3 keV band with the Neutron Star Interior Composition Explorer (NICER) and X-ray Multi-mirror (XMM)-Newton telescopes. In this band, X-rays from the source are dominated by the pulsed, surface thermal emission, enabling us to track the evolution of its spin ephemerides. During a particularly heavy-cadence observational period covering October 1 to November 27, we were able to employ a phase-coherent timing analysis, that is, tracking the time of arrival (TOA) of X-ray pulses from the source with a precise timing model. The pulse arrival time of SGR 1935+2154 from October 6 to November 27 is well predicted, with an accuracy that is a few per cent of the source spin-period, from a simple timing model that includes the frequency and its first and second derivatives. However, this model fails to predict the pulse arrival time from the 1st and the 2nd of October, showing an offset of about half a rotation just 3.5 to 5 days later. Attempting to model these residuals with the inclusion of higher-order frequency derivatives fails to provide a statistically acceptable fit (Fig. 1 and Methods).

Fig. 2 | Evolution of the temporal and spectral properties of SGR 1935+2154 during the 1 October 2020 to 27 November 2020 period. a, Phase residuals, in rotational cycles, of the SGR 1935+2154 X-ray pulses, according to the best-fit timing model that excludes the three earliest data points. Dashed line is the best-fit timing model to the full baseline, which includes a spin-down glitch (a sudden change to the spin frequency), along with its 1σ uncertainty (grey lines). The cyan horizontal line marks the time period during which FAST detected radio pulsations (Zhu et al., manuscript in preparation; W. Zhu, personal communication; I agree that manuscript in preperation is sufficient at this stage). Black dots and red squares represent the pulse phase of NICER and XMM-Newton data, respectively. In a and b, the horizontal lines on each data point indicate the temporal extent utilized to measure a pulse TOA, while in c, the horizontal lines represent the temporal extent utilized to derive the source pulsed fraction. **b**, Pulse residuals in seconds from the best-fit timing model, including the glitch, to the full baseline. c, The r.m.s. pulsed fraction of the X-ray emission in the energy range 1-3 keV derived by combining several individual observations, as shown with the horizontal bars. d, The 1-10 keV absorption-corrected flux from individual NICER and XMM-Newton observations. In all panels, the vertical dotted line is the occurrence of the CHIME bursts on 8 October 2020, while the vertical line on each data point is the 1σ uncertainty on those measurements. The XMM-Newton observation around day 40 is considered in tandem with the nearby NICER data when performing the timing analysis.

The sharp and large pulse-phase offset observed in the early October data is reminiscent of the glitching behaviour observed in pulsars and magnetars when they exhibit a sudden jump in spin frequency (that is, $\Delta \nu$) at a well-defined epoch $t_{\rm g}$. Indeed, a timing model that includes a glitch provides an accurate prediction of the pulse TOA for the full October and November time period (Figs. 2 and 3 and Table 1). In this model, we find that a frequency jump of $\Delta \nu=1.8^{+0.7}_{-0.5}\times 10^{-6}$ Hz(corresponding to a fractional change $\Delta \nu/\nu=5.8^{+2.6}_{-1.6}\times 10^{-6}$) occurred at a glitch epoch $t_{\rm g}=59,127.2^{+1.0}_{-0.7}$ modified Julian date (MJD) or October 5th. We note that the positive frequency jump is required to explain the early TOAs relative to our reference epoch (59,141.0 MJD), implying that the source experienced a negative $\Delta \nu$ frequency jump at $t_{\rm g}$. This abrupt slow-down



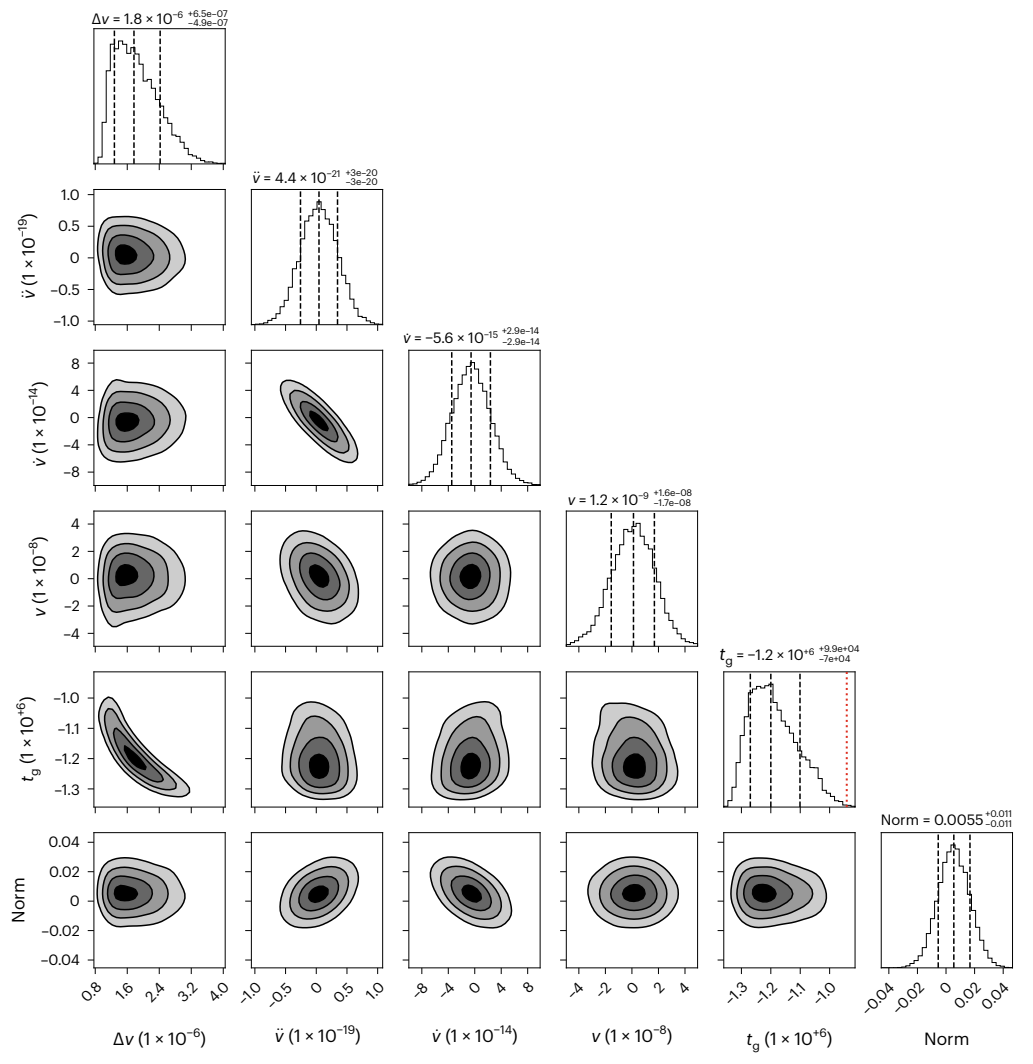


Fig. 3 | One- and two-dimensional posterior probability density distributions from a 10,000-step run of the emcee sampler of the parameters of our timing model (including a glitch). The full model includes six free parameters; ν , $\dot{\nu}$, $\ddot{\nu}$ and a normalization factor (Norm) that models the smooth evolution of the X-ray pulse arrival time, while $\Delta \nu$ and $t_{\rm g}$ are the sudden spin frequency jump and its epoch (in seconds from 19 October 2020), respectively. The positive anti-glitch is required to predict the earlier, October 1 and 2, data with respect to the timing

epoch, implying a sudden decrease of the spin frequency at $t_{\rm g}$, that is, an anti-glitch. Note that $\nu,\dot{\nu},\ddot{\nu}$ and Norm are relative to the best-fit model subsequent to the glitch epoch. In the one-dimensional histograms, the dashed lines represent the best-fit values along with their 1σ standard deviation. The dotted red line in the $t_{\rm g}$ histogram denotes the CHIME burst occurrence time. The two-dimensional grey regions, from dark to light, denote the 1σ , 2σ and 3σ , confidence contours on pair of parameter in the timing model.

is also evident when performing local spin frequency and spin-down measurements during the full October 1 to November 27 period (Fig. 4 and Methods). The corresponding loss of the magnetar's rotational kinetic energy due to this abrupt spin-down event is on the order of 3.0×10^{40} erg. This phenomenon of a spin-down glitch, also referred to as an 'anti-glitch', has been conclusively observed from one other magnetar, 1E 2259+586 (refs. 7,8). The spin-down-glitch magnitude, as well as the fractional change in the case of SGR 1935+2154, are about 1 order of magnitude larger compared with the 3 spin-down glitches observed so far from 1E 2259+586 over a period of 20 years of observations 8,9 . Other potential spin-down glitches have been reported from other magnetars, most notably the case of SGR 1900+14, where a spin-down event an order of magnitude larger than in SGR 1935+2154 occurred during an 80-day gap around the time of its August 1998 giant flare 10 .

We searched for X-ray variability in the properties of SGR 1935+2154 associated with the spin-down glitch epoch, but found none. For instance, the soft thermal and hard non-thermal X-ray flux throughout the October period remained at a constant level, as did the surface temperature and the non-thermal spectral shape (Figs. 2 and 5

and Supplementary Table 1). Moreover, the broad complex pulse profile shape, the pulsed fraction and the spin-down rate remained relatively stable throughout the same period (Figs. 6 and 4 and Supplementary Table 2). Finally, we detected no magnetar-like short bursts from SGR 1935+2154 in any of our X-ray observations, in line with the lack of detection of strong bursting activity by large-field-of-view hard X-ray instruments (for example, Fermi/Gamma-ray Burst Monitor (GBM), Swift/Burst Alert Telescope (BAT)). Any variability in the source-intrinsic X-ray flux associated with the glitch is either constrained to a 3σ upper limit of about 10^{-12} erg s⁻¹ cm⁻², based on a Nuclear Spectroscopic Telescope Array (NuSTAR) observation that occurred on 4 October 2020 (Supplementary Table 1), or confined to a 1-day interval between MJD 59,127.18, the end of the latter observation, and 59,128.06, the start of a NICER observation on October 6 (Fig. 7 and Methods).

While the spin-down glitch is apparently X-ray silent, SGR 1935+2154 exhibited profound changes at radio frequencies. First, three moderately bright FRB-like radio bursts were detected three days following the glitch epoch $^{\rm II}$. These bursts have a duration of about a few milliseconds each and occurred during a single rotational period of the

Table 1 | Best-fit spin parameters for the 1 October 2020 to 27 November 2020 period

Parameter	Value
RA (J2000)	19:35:41.64
Dec. (J2000)	21:54:16.9
Timescale	TDB
Ephemeris	DE405
Epoch (MJD)	59,141.0
v (Hz)	0.30789626(2)
ν̈ (Hz s ⁻¹)	-3.52(3)×10 ⁻¹²
ÿ(Hzs⁻¹)	1.9(3)×10 ⁻¹⁹
t_{g} (MJD, TDB)	59,127.2 ^{+1.0} _{-0.7}
Δ <i>v</i> (Hz)	$1.8^{+0.7}_{-0.5} \times 10^{-6}$
Valid range (MJD)	59,123.7–59,180.5
$\chi^2/d.f.$	15/13
r.m.s. residual (ms)	105
$\Delta v/v$	$5.8^{+2.6}_{-1.6} \times 10^{-6}$

Uncertainties on the derived parameters are presented in parentheses and represent the 1σ confidence interval.

source. These properties resemble those of the previous radio bursts detected from SGR 1935+2154, including the April 28 event^{6,12} (albeit much fainter). Less than one day following the radio-burst detections, the Five-hundred-meter Aperture Spherical Telescope (FAST) radio telescope observed SGR 1935+2154 and detected, for the first time, the emergence of a pulsed radio component¹³. This component was not detected in any of the numerous previous radio observations of the source¹⁴, including as recently as August 28 with the FAST radio dish.

The spin-down glitch may constitute a sudden transfer of angular momentum L away from the star, nominally carried by a particle wind along open field lines. This very likely originates from the surface of the star, yet it could be coupled to a release of magnetic energy stored in twisted magnetospheric field configurations ¹⁵. Other hypotheses for the origin of abrupt spin-down events exist. A sudden increase in the oblateness and/or moment of inertia I was a hypothesis used to explain the first anti-glitch observed for $IE 2259+586^{16}$. Alternatively, angular momentum transfer to a more slowly spinning inner crust could be a seed for strong spin-down ¹⁷. Yet, the contemporaneous detection of the spin-down glitch with the FRB-like bursts and the radio-pulsar episode appears remarkable, and suggests a causal connection given the rarity of each phenomenon (Methods). This is strongly suggestive of an external process, and so here we explore the wind scenario and its implications.

An ephemeral, strong wind emanating from the surface and passing through the magnetosphere on opened field lines will naturally generate strong angular momentum loss; such winds have been invoked to address general plasma loading of magnetar magnetospheres¹⁸. Using conservation of the total angular momentum L, for a magnetar of mass M, one deduces that the cumulative mass δm deposited in the wind satisfies $\delta m/M \approx 10^{-10}$ and a luminosity/mass-loss rate of $L_{\rm w} \approx 7 \times 10^{39} \, {\rm erg \, s^{-1}}$, under the assumption of a dipole near the surface and a putative transient wind duration of 10 hours (Methods). This mass loss should be considered an upper limit and is probably two to three orders of magnitude lower if the field configuration is strongly twisted near the poles, corresponding to a larger open-field-line polar cap that naturally arises during abrupt mass shedding¹⁸. In such a case, radiative efficiencies of a few per cent or less would then yield X-ray luminosities low enough to be consistent with the non-detection of any transient flaring activity associated with the glitch epoch (Methods).

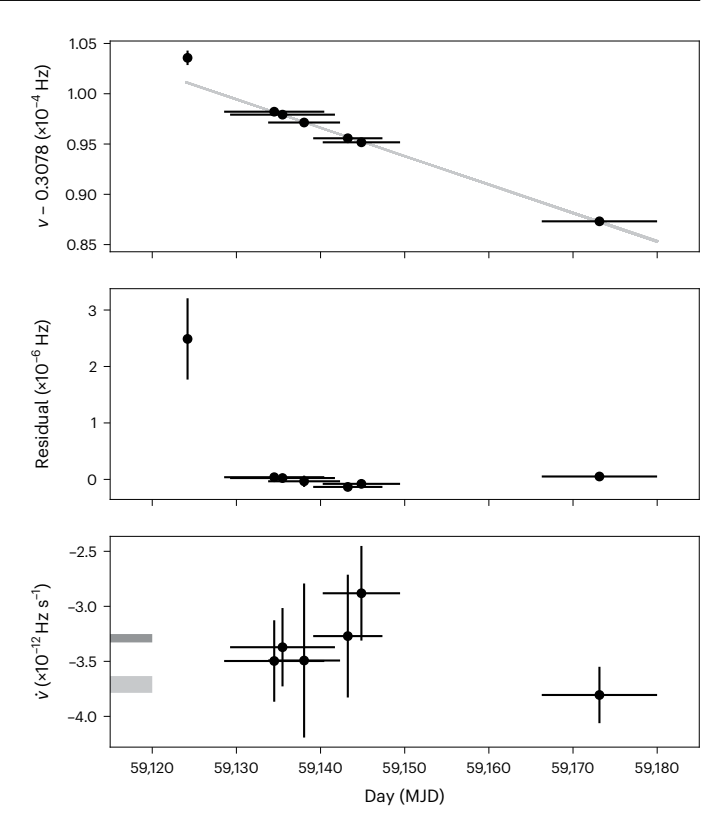
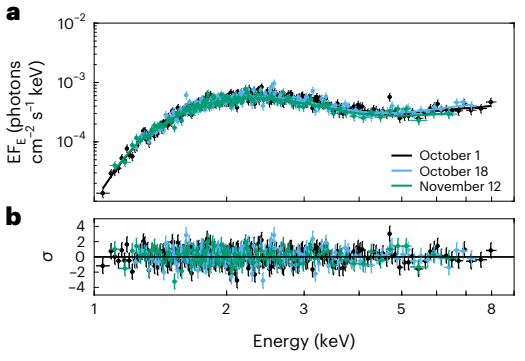
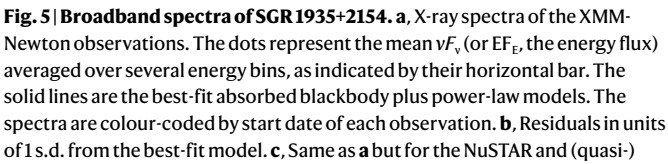


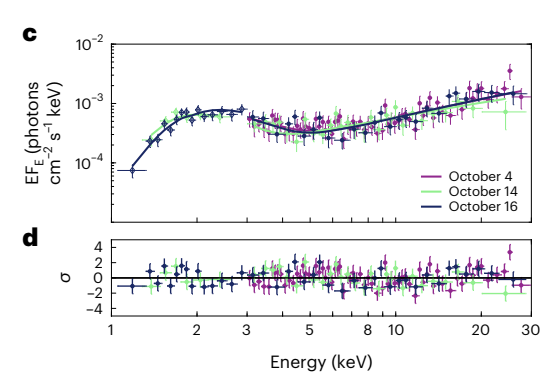
Fig. 4 | Evolution of the timing properties of SGR 1935+2154 from 1 October 2020 to 27 November 2020. The top panel shows spin frequency evolution as derived from phase-coherent timing analysis of mostly overlapping time segments spanning -2 weeks each (horizontal bars). The October 1–2 spin (leftmost data point) was derived independently. The middle panel is the same as above after subtracting a linear trend (solid grey line in the top panel) that best fits the 6 October 2020 to 27 November 2020 spin evolution. The lower panel shows the evolution of the spin-down rate measured from the same analysis. The light grey and dark grey bands are the spin-down rate and the corresponding uncertainty derived from phase-coherent analysis of heavy-cadence NICER observations covering 19 May 2020 to 6 June 2020 (ref. 3) and 18 June 2020 to 6 August 2020 (Supplementary Table 2), respectively. In all panels, the vertical line on each data point is the 1 σ uncertainty on those measurements. In some instances, the uncertainty is smaller than the symbol.

The extremely high opacity conditions during the strong wind phase generally preclude the establishment of electric potential gaps and associated electron acceleration, subsequent curvature radiation or resonant Compton upscattering, and electron–positron pair creation. These are all elements long deemed essential to radio emission in pulsars¹⁹, and most are likely for the generation of FRBs²⁰. Accordingly, one does not expect radio emission during the glitch. But what conditions prevail after this abrupt spin-down event that might permit FRB-like emission as well as the pulsed radio signal? The answer may lie in ephemeral modifications to the magnetic field geometry.

Powerful winds are well-known to comb out magnetospheric fields to become almost radial 21,22. The large mass loss of the strong wind implies that it probably originates at the stellar surface, probably connected to sub-surface structural rearrangements in the outer crust and its embedded fields. Such alterations may seed a temporary perturbation to the magnetospheric field morphology that may enhance conditions for pair creation and radio emission. Specifically, if the magnetic field curvature includes evolving toroidal (twisted) components that are vestiges of the powerful wind phase, the pair-creation rate can be increased substantially relative to that for photon splitting (Methods). This prospect is underpinned by the extreme sensitivity of the pair-creation rate to the magnetic field strength, the field-line







simultaneous NICER observations. The colours represent the start date of each NuSTAR observation. The diamonds in the right panel represent the NICER data, while the points are for NuSTAR. ${\bf d}$, Residuals in units of 1 standard deviation from the best-fit model. No statistically significant variability in the spectral shape is detected. In all panels, the vertical line on each data point is the 1σ uncertainty on those measurements.

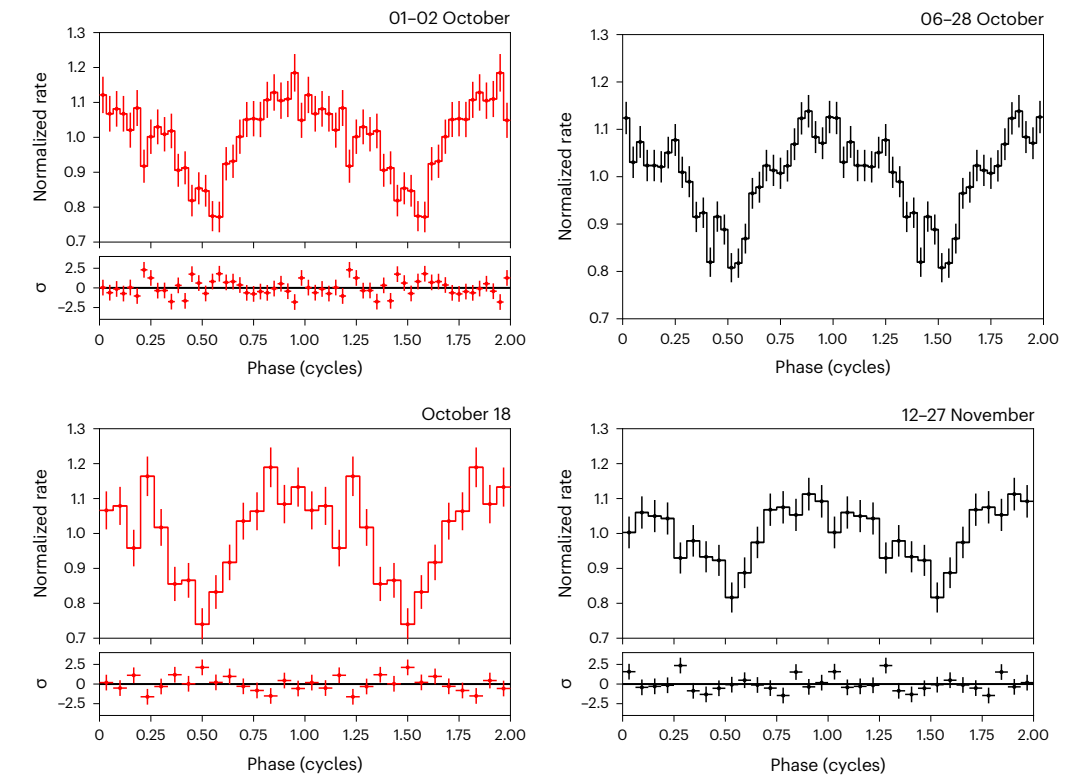


Fig. 6 | **Pulse profiles in the 1–3 keV energy band at different epochs during our October/November monitoring.** These are folded utilizing the timing solution presented in Table 1. Time is indicated at the upper-right corner of each panel. Two cycles are shown for clarity. The red profiles were constructed from XMM-Newton-only data, while the black profiles are from NICER. The source pulse profile from the XMM-Newton November 12 observation is poorly constrained due to low S/N and hence not shown. Notice the complexity of the

profile, especially during October 6 to 28, which boasts the largest S/N. The lower panels of the XMM-Newton and the NICER November profiles are their respective deviation, in units of σ , from the high S/N October 6 to 28 NICER profile, indicating no notable variability in the pulse shape throughout the validity period of our timing solution. In all panels, the vertical line on each data point is the 1σ uncertainty on those measurements. The horizontal lines represent the phase-bin sizes.

curvature and the directional beaming of radiation^{23,24}. As the wind further abates, the twisted and curved field lines re-establish themselves at their pre-glitch configuration so that photon splitting again becomes more potent in suppressing pair creation²⁵, probably shutting down the radio signal.

Such field geometry adjustments (see Supplementary Fig. 1 for a depiction) cannot be sufficient to modify the surface thermal emission below 4 keV (for example, through particle bombardment 26) and

the hard X-ray tail signal above -4 keV, since these are not impacted by the spin-down glitch (Fig. 5). Yet this change may be confined to polar locales and just enough to permit the triggering of radio bursts 20,27 and pulsed radio emission. These may accompany a residual wind phase at a modest level commensurate with the long-term spin-down rate, with relaxation due to Ohmic dissipation back to the long-term field configuration in concert with the radio turn-off a month later. In essence, perhaps the spin-down glitch temporarily moves the radio 'death line'

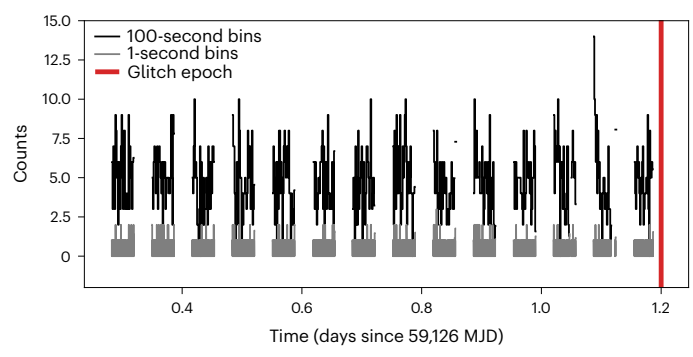


Fig. 7 | The October 4 NuSTAR light curve of SGR 1935+2154 in the 3–30 keV range. The grey and black histograms display two different binnings of the light curve at 1- and 100-seconds resolution, respectively. The red vertical line denotes the best-fit glitch epoch at 59,127.2 MJD. Note that the NuSTAR observation covers the 1σ lower limit on the glitch epoch.

on the pulsar period–period-derivative diagram²⁸ to longer periods due to its field geometry modifications. The persistent surface X-ray signal emanating from a considerable range of closed field-line colatitudes just continues unaltered and unabated. Our results highlight the necessity for deeper theoretical studies of field morphology associated with magnetospheric plasma loading and its evolution via Ohmic dissipation, in concert with gamma-ray opacity and pair-creation considerations to unravel the physical conditions and mechanisms responsible for FRB-like bursts and pulsed radio emission in magnetars.

Methods

NICER observations and data reduction

NICER²⁹ is a soft X-ray telescope mounted on the International Space Station, sensitive to photon energies in the range 0.3-12 keV. It consists of 56 co-aligned X-ray concentrating optics, of which 52 are currently operational, providing a collecting area of about 1,900 cm² at 1.5 keV. SGR 1935+2154 was observed extensively with NICER following the announcement of the 8 October 2020 Canadian Hydrogen Intensity Mapping Experiment (CHIME) radio bursts. For this Article, we analyse the NICER observation IDs 3020560154-75 and 3655010401-02, covering the period 6 October 2020 to 27 November 2020, during which a detailed spectral and phase-coherent timing analysis is carried out (see below). We note that two observations that occurred on 2020 December 3 and 4 (IDs 3020560176 and 3020560177) resulted in a combined exposure of 2 ks after background cleaning, which is insufficient for any meaningful spectral or temporal analysis, hence, they are ignored. We also perform detailed timing analysis on heavy-cadence NICER observations covering the 18 June 2020 to 6 August 2020 period (observation IDs 3655010302-03 and 3020560120-48). Between these two episodes, however, only sparse and short X-ray observations existed, which prevented us from phase-coherently connecting them to the focal epoch of this paper. In addition, subsequent to November, SGR 1935+2154 could not be observed for two months due to its proximity to the Sun. For the observations included in our analysis, we use NICERDAS version v.008c to create cleaned and calibrated event files, extract spectra and build light curves, after applying standard filtering to all observations as described in the NICER Data Analysis Guide (https://heasarc.gsfc. nasa.gov/docs/nicer/dataanalysis/niceranalysisguide.html). Finally, we estimate the background number counts per NICER-energy channel utilizing the nibackgen3C50 tool, and add a conservative 20% systematic uncertainty to this estimate³⁰.

XMM-Newton observations and data reduction

XMM-Newton is an imaging X-ray satellite with several cameras on board, sensitive to photon energies in the range 0.4–10 keV. For this Article, we analyse the XMM-Newton observations taken on 1 October

2020 (observation ID 0871191301), 18 October 2020 (observation ID 0872390601) and 12 November 2020 (observation ID 0872390701). with background-corrected exposures of 61, 29 and 18 ks, respectively. We focus on the European Photon Imaging Camera-pn camera³¹, which operated in prime full-frame mode for all observations, affording a 73 ms time resolution. We performed the cleaning and filtering of the events using the XMM-Newton Science Analysis Software (SAS) version 19.1.0. We applied standard filtering to all observations similarly (for example, only good X-ray events with patterns 0-12 were accepted). Furthermore, we excluded intervals of high background flaring activity, for example, due to solar flares, as measured from source-free full field-of-view light curves. Finally, we extracted source events from a circle centred at the best-fit point-spread function location as obtained with the SAS task eregionanalyse, having a radius of 60", encapsulating 90% of a point-source point-spread function. Background events are extracted from a source-free annulus centred at the source with inner and outer radii of 120" and 200", respectively. We generated response matrix and ancillary files using the SAS tasks rmfgen and arfgen, respectively.

NuSTAR observations and data reduction

The focusing hard-X-ray telescope NuSTAR 32 consists of two identical modules, focal plane module A and focal plane module B, sensitive to photon energies in the range 3–79 keV. NuSTAR observed SGR 1935+2154 on 4 October 2020 (observation ID 80602313008), 14 October 2020 (observation ID 90602332002) and 16 October 2020 (observation ID 90602332004) with exposures of 40, 20 and 18 ks, respectively. We reduced the NuSTAR data using NuSTARDAS software version 2.1.1 as part of HEASoft 6.29c along with the calibration files version 20201130. We extract source events, light curves and spectra from a circular region with a 45″-radius around the source-central brightest pixel. We estimate the background contribution to the source from an annulus centred on the source, with inner and outer radii of 120″ and 200″, respectively.

Timing analysis

We converted all cleaned events time stamps to the Barycentric Dynamical Time (TDB), which measures the photon arrival times at the solar system barycenter. For this purpose, we utilized the JPL ephemerides DE405, and the best-known source location as measured with the Hubble Space Telescope³³. The source small-pulsed fraction of around 8% and its relative faintness proved problematic to maintaining phase coherence throughout the extent of the 2020 observations. Nevertheless, the heavy X-ray cadence and deep observations throughout the months of October and November (October 1 to November 27) allowed us to follow the pulse TOA with high accuracy. First, we relied on the XMM-Newton and NICER observations of October 18 and 19, with an exposure totalling 72 ks to establish an accurate spin frequency of the source. Using a Z_n^2 test³⁴ with number of harmonics n = 2, we find the strongest signal in the energy range 1-3 keV at a frequency v = 0.3078961(4) Hz at the epoch $T_0 = 59,141.0$ MJD (TDB). Using these ephemerides, we measured the pulse arrival time for segments of data from October 1 to November 27 containing approximately 6,500 events; the number of events required to detect the pulsed emission at ~4.5 σ . We employed a non-binned maximum likelihood technique to measure the pulse TOA^{35,36}. We relied on the above high signal-to-noise ratio (S/N) pulse profile to build a model of the pulse shape, consisting of the sum of the first two harmonics of a Fourier series. We then fit this model to each unbinned data segment, allowing for a phase shift $\Delta \phi$. The 1σ uncertainty on the phase shift was established by using the Markov chain Monte Carlo (MCMC) sampler emcee³⁷. We assumed a flat prior $\Delta \phi \in [0, 2\pi)$ and evolved 32 walkers for 1,000 steps.

The pulse arrival time from October 6 to November 27 can be well fit with a simple model for pulse evolution following

$$\phi(t) = \phi_0 + v(t - t_0) + \frac{1}{2}\dot{v}(t - t_0)^2 + \frac{1}{6}\ddot{v}(t - t_0)^3 + \dots$$
 (1)

truncated at the second frequency derivative term \ddot{v} , where t is time and t_0 is the spin ephemerides epoch. Yet, the pulses from the early October XMM-Newton observation, which starts 5 days and ends 3.5 days before the NICER October 6 observation, are offset from the simple timing model by more than half a rotation (Fig. 2). The above simple model evidently fails to predict these pulse phases. Hence, we added a fourth term (\ddot{v}) and fit the phase offsets; this too does not result in a satisfactory fit, showing strong residuals throughout the baseline (Fig. 1, left panels). This model results in a reduced χ^2 of 3.2 for 14 degrees of freedom (d.f.). Simultaneously adding a fourth and a fifth (\ddot{v}) term to equation (1) improves the quality of the fit somewhat, resulting in a reduced χ^2 of 2.7 for 13 d.f., while strong phase residuals are still evident (Fig. 1, right panels).

The large and sharp October 1st and 2nd TOA offset of more than half a cycle and the inadequacy of describing the full baseline utilizing a smooth timing model (even when instantaneously adding two extra terms to equation (1)) is strongly suggestive of an abrupt change to the spin frequency ν , that is, a glitch. To test this hypothesis, we added a glitch model to the smooth pulse-arrival-time evolution that described the October 6 to November 27 TOAs, whereas at $t < t_{\rm g}$

$$v(t) = v_t + \Delta v. \tag{2}$$

Here $t_{\rm g}$ represents the glitch epoch, $v_{\rm t}$ is the predicted spin frequency subsequent to the glitch and Δv is the frequency jump at $t_{\rm g}$. The best-fit model that describes the data is shown as a dashed black line in Fig. 2. This model results in a reduced χ^2 of 1.15 for 13 d.f., largely preferable to the above two timing models. Note that this model has the same number of parameters as the continuous one with frequency derivatives up to \ddot{v} . It is also fully consistent with the radio timing solution as derived with FAST at the 1σ level (Zhu et al., manuscript in preparation; W. Zhu, personal communication; I agree that manuscript in preperation is sufficient at this stage). We sample the full parameter space of this model through the emcee MCMC sampler, assuming flat-prior probability densities of all parameters and evolving 32 walkers for 10,000 steps. We also exclude 500 burn-in steps. The one- and two-dimensional posterior probability densities are shown in Fig. 3.

We checked the constancy of the pulse profile shape throughout the validity period for our timing solution, most importantly to ensure that the October 1 and 2 pulse-arrival-time deviations are not due to such variations. For this, we subtracted the October 1st/2nd XMM-Newton pulse profile from the high S/N October 6 to 28 NICER profile. We performed the same operation on the October 18 XMM-Newton profile and the November NICER profile. All the residuals are consistent with a horizontal line model (y = constant) having a reduced $\chi^2 \approx 1$. This is demonstrated in Fig. 6, where we show the deviations, in units of σ , of these profiles from the high S/N one. Hence, we safely conclude that a change in the pulse shape cannot be attributed to the pulse-arrival-time residuals.

As an extra layer of verification of our results, we performed another set of timing analyses. Over the 6 October 2020 to 27 November 2020 time period, we independently generate a phase-coherent timing solution of mostly overlapping time segments spanning ~2 weeks each. From this timespan we derive a set of $\nu - \dot{\nu}$. We also independently derive the source spin frequency during the XMM-Newton October 1 data, first from a \mathbb{Z}_2^2 search, then refining it through a phase-coherent analysis. These results are summarized in Fig. 4. The upper panel shows the spin evolution while the middle panel presents the residuals after subtracting a linear trend that best fits the October 6 to November 27 data (shown as a grey solid line in the upper panel). The October 1 spin frequency is evidently incompatible with the extrapolation of the October 6-November 27 spin evolution at the $\gtrsim 3\sigma$ level, with $\Delta v = 2.4(7) \times 10^{-6}$ Hz. Note that the second largest deviation from the linear trend is 1.4×10^{-7} Hz. This independent measurement of Δv is consistent with the full phase-coherent analysis and, indeed, implies an abrupt slow-down on the timescale of <3.5 d.

Few magnetars are known to exhibit extreme timing noise, especially in the months following a major outburst, for example, 1E 1048.1–5937 (ref. 38) and Swift J1818.0–1607 (ref. 39). In these cases, the spin-down rate erratically varies over the course of several months, reaching a maximum of around an order of magnitude larger than the nominal value. This is in contrast to the case of SGR 1935+2154. As we show in the lower panel of Fig. 4, the spin-down rate for the two months following the spin-down glitch shows very little variability, constrained to ≤20%. We also derive, through a phase-coherent analysis, the spin ephemerides from a heavy-cadence NICER observing run covering 18 June 2020 to 6 August 2020 (Supplementary Table 2 and dark grey bar in the lower panel of Fig. 4), and show the spin-down rate measured from 19 May 2020 to 6 June 2020 (ref. 3) (light grey bar). The \dot{v} for both epochs are consistent with the spin-down rate measured during the later 2020 period, implying that the source shows low-level timing noise over longer timescales of months.

Using the best-fit timing model for the full period, we measure the root-mean-square (r.m.s.) pulsed fraction in the energy range 1–3 keV of several combined NICER datasets to boost the S/N and individual XMM-Newton observations using a Fourier series consisting of two harmonics⁴⁰. We find a stable pulsed fraction of around $(9\pm1)\%$ (Fig. 2c). We find no strong pulsed emission at energies >3 keV in either instrument, nor did we find any pulsed emission in NuSTAR. For the October 1 data, which boasts the highest S/N at energies >3 keV, we derive a 3σ upper limit of 12% on the pulsed fraction at energies 3–10 keV. We also built a NICER pulse profile for the October 6 to 28 period, which overlaps with the radio-pulsar period (Fig. 6). We note the complexity of the profile. The multitude of peaks and their spread across rotational phase are highly indicative of large portions of the star surface being activated.

Spectral analysis

Utilizing the grppha command within HEASOFT, we group the XMM-Newton and NuSTAR spectra to have at least 30 counts per energy bin, and 5 counts per energy bin for NICER. We fit the 3 XMM-Newton spectra in the 1-9 keV range simultaneously with a combination of a thermal blackbody and power-law components, both affected by interstellar absorption. We leave all model parameters free to vary, except for the hydrogen column density $N_{\rm H}$ of the interstellar absorption model. As shown in Fig. 5, the model describes the data well with no clear systematic residuals. The reduced χ^2 is approximately 1.0 for 730 d.f. The best-fit model parameters along with their uncertainties are summarized in Supplementary Table 1. There is no notable variation in any of the model parameters between the three epochs, albeit sampling the full October and November time period, which coincide with the pre-glitch, post-glitch and radio turn-on, and the radio turn-off of November. This demonstrates the stability of the soft and hard X-ray-emitting region throughout the glitch/radio-on time interval.

We fit the NuSTAR spectra of the 3 different observations to the same model as above in the 3 keV to 30 keV energy range. We supplement the NuSTAR spectrum of October 16 with a simultaneous NICER observation (observation ID 3020560159), and the one from October 14 with a quasi-simultaneous NICER observation (observation ID 3020560158) taken 22 hours before. We link the hydrogen column density amongst all spectra while allowing the rest of the model parameters to vary. The model adequately fits the data with a reduced χ^2 of 0.9 for 659 d.f. We summarize the spectral results in Supplementary Table 1. The NuSTAR+NICER spectra confirm the stability of the thermal and non-thermal components. The October 4th NuSTAR observation, which ended at the best-fit glitch epoch, places stringent constraints on the timescale of any induced radiative variability.

Finally, we fit the individual NICER observations to the same model as above in the 1 keV to 5 keV energy range. The NICER spectra cannot constrain the power-law component due to the low S/N at energies >3 keV. Hence, we fixed the power-law model parameters to those of XMM-Newton. Moreover, we linked the blackbody temperature

between all spectra since it shows no sign of considerable variability. We present the 1–10 keV flux evolution throughout the full October and November period in Fig. 2.

Burst searches

We employ a Poisson methodology to search for any bursts in all of our datasets^{3,41}. In summary, using a 32 ms binned light curve, we flag any deviation from the average count rate in a single observation that cannot be ascribed to random Poisson fluctuation. We then scrutinize these bins to eliminate spurious detections, for example, due to flaring background. We do not find any bursts with significance >5 σ in any of the observation. We repeated our procedure for different timescales, namely, 64, 128, 512 and 1,024 ms and found no burst-candidates. The average NICER count rate of SGR 1935+2154 in the 1–8 keV range is -0.7 counts per second. Assuming a top-hat burst with duration of 1 s, we place a 5σ detection upper limit of about 8 counts per second, which translates to an absorption-corrected flux of 10^{-10} erg s⁻¹ cm⁻² assuming $N_{\rm H} = 2.2 \times 10^{22}$ cm⁻² and a blackbody spectrum having a temperature kT = 1.5 keV, where k refers to Boltzmann constant³. At a distance of 10 kpc (ref. 42), this implies a burst luminosity of 10^{36} erg s⁻¹.

Chance alignment of an anti-glitch, radio bursts and pulsed radio episode

Due to the lack of years-long monitoring of SGR 1935+2154 with either X-ray or radio facilities and our poor knowledge of the waiting-time distribution of any of these phenomena, we do not attempt to provide a quantitative measurement of the probability of the three events occurring within few days of one another. Rather, we provide a qualitative description of their occurrence rate and argue of their individual rarity.

SGR 1935+2154 has been coherently timed on two occasions, 2014 July–2014 November¹ and our current epoch covering 2020 October–November, for a total of 180 days. Any spin-down glitch with a magnitude similar to the one presented in Table 1 would be easily detectable during the above 2 periods, implying a rough upper limit of one spin-down glitch every 0.5 years. We also note that such events are exceedingly rare within the magnetar population, having been conclusively detected in only one other magnetar, 1E 2259+586. In the latter, 3 such events have been detected in the course of 20 years of monitoring³,9 implying a rate of at most 1 in 6 years.

The CHIME radio dishes have good daily coverage of SGR1935+2154 totalling 15 minutes. Including the detection of the FRB on April 28, this translates to a rate of roughly 4×10^{-4} radio bursts per CHIME-day in 2020 (less if one considers CHIME observations in 2018 and 2019, yet SGR1935+2154 was mainly quiet during these years). Again, note that this assumes a Poisson process. From continuous radio observations of SGR 1935+2154 in the weeks and months following the April 28 event, it is evident that these radio bursts are rare and highly clustered 12,14,43 . With this caveat in mind, we derive a joint probability of about 10^{-5} that the anti-glitch and the CHIME bursts occur within a 3-day period, corresponding to a 4.2σ chance coincidence.

The faintness and narrow frequency range of the SGR 1935+2154 radio pulsed emission makes it difficult to detect with radio dishes apart from FAST (Zhu et al., manuscript in preparation; W. Zhu, personal communication; I agree that manuscript in preperation is sufficient at this stage). Nevertheless, FAST performed regular observations of SGR 1935+2154 between 15 April 2020 and 14 July 2021 at a cadence varying from once per day to about once per month. The only period with a pulsed radio detection is October 9 to 28. The earliest FAST observation to the radio turn-on occurred on 28 August 2020, that is, 35 days before our spin-down glitch epoch.

The transient nature of the pulsed radio emission in magnetars argues that it must be triggered by a certain event, which probably causes magnetospheric modifications connected to the open-field-line region. The SGR 1935+2154 long-term light curve does not show any notable change to the X-ray spectral properties in 2020 August and

September^{3,44}, nor were there any reported hard X-ray bursts from large-field-of-view telescopes, for example, Fermi/GBM or Swift/BAT. The only notable anomaly in this time period is the spin-down glitch. Hence, while it is impossible to prove that no radio pulsations occurred during the radio-dark 35-day interval, the fact that the spin-down glitch is the only notable spectral or temporal anomaly surrounding the observed radio activation is strongly suggestive of an association of these two exceedingly rare events, rather than them being chance coincidences.

Ephemeral wind interpretation

We explore here how mass loss through a transient, strong wind that extracts angular momentum from the star is constrained through the spin-down glitch. Such an external process is perhaps a most natural interpretation in considering physical connections of an abrupt spin-down to an incipient radio signal. A sudden (small) increase in stellar oblateness in dimensions perpendicular to the spin axis could explain the anti-glitch, which could be affected by a changing magnetic 'buoyancy' in the crust¹⁶. On its own, it is unclear how this would precipitate a magnetospheric radio signal. Yet, it could arise in conjunction with a magnetic energy release near the poles that drives a wind that we now describe.

The basic geometry of the wind and stellar configuration is depicted in Supplementary Fig. 1. Let $\delta m \approx \dot{m} \delta t$ be the cumulative mass shed in time δt , putatively at an approximately constant rate \dot{m} , on field lines with footpoints very near the magnetic pole. If the inclination angle between the magnetic and rotation axes is α , then $R\Omega\sin\alpha$ is the circular rotation speed at altitude R above the magnetic pole ($\Omega = 2\pi v$ = $2\pi/P$ is the angular rotation frequency). Therefore, the angular momentum shed is on the order of $\delta mR^2\Omega\sin\alpha$. As the wind flows out towards the light cylinder, the star continues to transfer angular momentum to the wind until the magnetic energy density drops below that of the plasma at $R \approx R_{eq}$. Subsequently, the wind combs the field lines out and the wind's angular momentum decouples from the stellar rotation. The net angular momentum transfer from the magnetar to the wind is $\delta L_{\rm w} = \delta m R_{\rm eq}^2 \Omega \sin \alpha$: it can be equated to $I |\delta \Omega|$, where $\delta \Omega$ is the abrupt change in the rotation frequency measured by the timing data. Assume that the star's moment of inertia $I = 2\epsilon MR_{ns}^2/5$ is essentially constant during the shedding event, where ε represents the departure from a uniform density sphere and R_{ns} is the neutron star radius. Thus

$$\frac{\delta m}{M} \approx \frac{2\epsilon}{5} \frac{R_{\rm ns}^2}{R_{\rm eq}^2} \frac{|\delta \Omega|}{\Omega \sin \alpha},\tag{3}$$

where *M* is the neutron star mass. The spin-down glitch establishes that $-\delta\Omega/\Omega=5.8\times10^{-6}$.

To determine the equipartition radius $R_{\rm eq}$ at which the plasma energy density begins to exceed the magnetic field energy density $B^2/8\pi$, presume that the wind flows with a mean wind speed of $\beta_{\rm w}c$, with $\beta_{\rm w} \lesssim 0.8$ that is mildly relativistic and where c is the speed of light. At altitude $R_{\rm eq}$, the cross-sectional area of the open-field-line flux tube is $A=\pi R_{\rm eq}^2\theta^2$, with $R_{\rm eq}/\theta^2\approx R_{\rm lc}=Pc/2\pi$, where P is rotation period, defining the local colatitude θ (\ll 1) of the last open field line in a dipolar geometry, and $R_{\rm lc}=Pc/2\pi$ is the light cylinder radius. Note that plasma loading of the magnetosphere will enlarge this area of open field lines 18 . The mass flux through this area couples to the mass density ρ via the conservation relation $\dot{m}=\rho A\beta_{\rm w}c$. Equating ρc^2 to $B^2/8\pi$ at altitude $R_{\rm eq}$ gives $\rho\!\rightarrow\!\rho_{\rm eq}$, and

$$\rho_{\rm eq}c^2 \approx \frac{\dot{m}c^2P}{2\pi^2R_{\rm eq}^3\beta_{\rm w}} \approx \frac{B_{\rm p}^2}{8\pi} \left(\frac{R_{\rm ns}}{R_{\rm eq}}\right)^6. \tag{4}$$

Here B_p is the surface polar field strength. This constrains R_{eq} , and when combined with the angular momentum budget equation in equation (3) to eliminate δm yields

$$\frac{R_{\rm eq}}{R_{\rm ns}} \approx \left(\frac{\pi}{4} \frac{B_{\rm p}^2 R_{\rm ns}^3 \beta_{\rm w}}{\delta m c^2} \frac{\delta t}{P}\right)^{1/3} \approx \lambda \frac{\Omega}{|\delta \Omega|} \frac{B_{\rm p}^2 R_{\rm ns}^3}{M c^2} \frac{\delta t}{P},\tag{5}$$

with $\lambda = (5\pi/8\varepsilon)\beta_w \sin\alpha$. Inserting this into equation (3) delivers the fractional stellar mass $\delta m/M$ lost to the ephemeral wind. Evaluation for a transient wind duration of 10 hours yields

$$\frac{\delta t}{P} = 1.1 \times 10^4 \rightarrow \frac{R_{\rm eq}}{R_{\rm ns}} \approx 150$$
 and $\frac{\delta m}{M} \approx 10^{-10}$. (6)

This estimate assumes that $\lambda \approx 1$ and that $\varepsilon/\sin\alpha = 1$. The result is a modest fractional mass loss (that is, -2.5×10^{44} erg in total energy with a wind luminosity of $L_{\rm w} \equiv \dot{m}c^2 \approx 7 \times 10^{39}$ erg s⁻¹) that implies that spin-down glitches can be recurrent events on timescales of 10 years or more for magnetars throughout a putative 10^4 -year lifetime. Their polar confines suggest a precipitating event somewhat akin to volcanism, spewing out plasma at mildly relativistic speeds. This could be driven via disruptive magnetic stress and energy release in the crust. In contrast, rapid mass loss on a timescale of a few minutes $(\delta t/P = 10^2)$ implies that $R_{\rm eq} \approx 1.5 R_{\rm ns}$ and $\delta m/M \approx 10^{-6}$ for $M = 1.4 M_{\odot}$. This circumstance essentially approximates a structural rupturing of the outer crust, with a wind luminosity of $L_{\rm w} \approx 7 \times 10^{45}$ erg s⁻¹ that is comparable to the radiative luminosity of the 'initial spike' of a magnetar giant flare.

The above calculations constitute an approximate upper bound to the mass loss and wind luminosity for fixed δt . The dipole configuration used therein is an idealized choice that needs to be adapted to treat more realistic descriptions of plasma-loaded magnetospheres such as in pulsar plasma simulations^{21,22} and magnetar analytic models¹⁸. The upshot of plasma loading is that it expands the zone of open field lines, so that the dipole form $\theta \approx [R_{eq}/R_{lc}]^{1/2}$ is an underestimate for θ , and reduces the size of the magnetosphere. Without introducing extra parametric complexity, the quickest way to get a sense of this plasma-driven opening of the magnetosphere is to note that it is akin to shortening the rotation period *P*. Thus, for example, lowering *P* in equation (5) by a factor of 10 increases R_{eq} by the same factor and then reduces the net mass loss in equation (3) by two orders of magnitude, and accordingly would result in $L_w \approx 7 \times 10^{37}$ erg s⁻¹ for $\delta t = 10$ h. This drop is driven by the lower densities in equation (4) required to realize a given angular momentum shed at high altitudes. Accordingly, plasma-loading influences on the field structure, and likewise twist modifications, will generally lower the average mass-loss rates.

Opacity of the wind

Such a dense wind has the potential to occult the surface and magnetospheric signals, yet the NuSTAR and NICER observations indicate that such an obscuration is not important. One can quickly estimate the lepton number density $n_{\rm e} = \rho/m_{\rm e}$ (where $m_{\rm e}$ is the electron mass) in a pure pair plasma in the wind zone out to any radius $R \lesssim R_{\rm eq} \ll R_{\rm lc}$ along the open field lines. For the plasma, the flared wind solution $A = \pi R^2 \theta^2$, with $R/\theta^2 \approx R_{\rm lc} = Pc/2\pi \approx 1.5 \times 10^{10}$ cm, yields a radial dependence of $\rho = \rho_{\rm eq}(R_{\rm eq}/R)^3$. The non-magnetic Thomson opacity $\tau_{\rm T} = n_{\rm e}\sigma_{\rm T}R$, appropriate for the sub-critical fields at $R \gtrsim 10R_{\rm ns}$, can be developed using equation (4), yielding

$$\tau_{\rm T} = \sigma_{\rm T} R_{\rm ns} \frac{B_{\rm p}^2}{8\pi m_{\rm e} c^2} \left(\frac{R_{\rm ns}}{R_{\rm eq}}\right)^5 \left(\frac{R_{\rm eq}}{R}\right)^2, R \lesssim R_{\rm eq},$$
 (7)

where σ_T is the non-magnetic Thomson cross-section. For the wind configuration given by equation (6), this pair plasma result evaluates to $\sim 8.2 \times 10^4$ at $R_{\rm eq}$, that is, an extremely high opacity, and the wind remains opaque out to beyond the light cylinder. If instead the plasma is hydrogenic, the optical depth is reduced by a factor of $m_{\rm e}/m_{\rm p}$ (where $m_{\rm p}$ is the proton mass), yielding $\tau_T \approx 50$ at $R_{\rm eq} \approx 150 R_{\rm ns}$. For either hydrogenic or pair plasma, τ_T is extremely large at the stellar surface.

The ephemeral wind will clearly obscure any background radiation field from the surface or inner magnetosphere that impinges upon it. Yet, the solid angle of the wind at R_{eq} is small. Its effective area at this radius is $A = \pi R_{\rm eq}^2 \theta^2 \approx \pi R_{\rm eq}^3 / R_{\rm lc}$, constituting a solid angle of $\sim \pi R_{\rm eq}/R_{\rm lc} \approx 3 \times 10^{-2}$ steradians, corresponding to $\theta \approx 5.7^{\circ}$ for the dipole, and larger for field geometry modifications due to plasma loading. Above R_{eq} , the wind combs out the field and propagates radially, so its solid angle is approximately preserved out to the light cylinder. Thus, wind occultation of the persistent emission from low altitudes or the surface is relatively small, even though the wind will remain optically thick out to R_{lc} . In the putative subsequent residual wind phase, when observations are resumed, $|\delta\Omega|$ is much smaller than during the anti-glitch. The value of \dot{m} is probably at least 3-4 orders of magnitude smaller, $R_{\rm eq}$ increases by a factor of 10–20 and it can be quickly shown that while the solid angle of the residual wind is large near the light cylinder, this more benign wind is transparent to Thomson scattering there.

Conditions for pair creation

The historical paradigm that an abundance of electron–positron pairs is required for persistent radio emission in pulsars ¹⁹ still prevails. Radio pulse profile and polarization constraints indicate that the altitude of radio emission ^{45,46} is generally in the 100–1,000 km range, and is presumed to occur over the magnetic poles. During the strong ephemeral wind epoch, the opacity is so enormous that it precludes the formation of electric potential 'gaps'. These potentials seed primary electron acceleration and subsequent curvature radiation that lead to quantum electrodynamics magnetic pair creation $\gamma \rightarrow e^+e^-$ and ultimately cascading ⁴⁷. After the strong wind phase has ceased, the opacity drops precipitously and electric potentials can stably exist, so that pair creation and radio emission may become possible.

As $\gamma \rightarrow e^+e^-$ has a fundamental energy threshold of $2m_ec^2\sin\theta_{kB}$, where θ_{kB} is the angle of gamma-ray propagation relative to the local field direction, magnetic photon splitting $\gamma \rightarrow \gamma \gamma$ can be a prolific competitor in magnetars^{24,25} since it has no such threshold. In a first examination of this possibility, Baring and Harding²⁵ concluded that suppression of pair creation by photon splitting is efficient in magnetars and could explain why no radio magnetars had been detected before 2000 and only a handful of transient ones since, SGR 1935+2154 being the latest. Yet the balance in the competition between pair conversion and splitting of gamma-rays depends on the inner magnetospheric emission locale in magnetars, with splitting tending to dominate in polar regions where a dipolar field is stronger and pair creation being favoured in non-polar locales where the field-line radius of curvature is smaller⁴⁸.

During the strong polar wind phase, the magnetic field lines are combed out radially above $R_{eq} \gtrsim 15R_{ns}$, similar to that evinced in pulsar magnetosphere simulations^{22,49}. Vestiges of this field structure will persist for some time after the anti-glitch. On the long term, magnetars are believed to possess globally twisted fields with toroidal components generated by surface and magnetospheric currents⁵⁰. In the domain of very strong twists, the field morphology approaches a split monopole and therefore resembles plasma-loaded magnetospheric geometry. The introduction of strong twists moves the zones of dominance by pair creation by gamma-rays of energies ≥50 MeV more towards the poles and to slightly higher altitudes 51 ~ $10R_{ns}$ to $30R_{ns}$, which are still below the putative locales for radio emission. This change is precipitated by the extreme sensitivity of the pair-creation rate to the field strength |B| and curvature of magnetic field lines, and the direction of gamma-rays relative to **B** (refs. 23–25). Thus, we anticipate that polar pair creation and pulsed radio emission can proceed after the strong wind abates significantly. Yet Ohmic dissipation of toroidal/twisted fields in magnetars is nominally on the timescale of months to years⁵², depending on the voltage along the pertinent field lines. Presuming that a similar relaxation transpires in the decaying wind scenario here, photon splitting will eventually again dominate in polar colatitudes⁴⁸ after sufficient untwisting, and magnetic pair creation and radio emission there will cease. The magnetic evolution must be largely confined to the polar regions so as to not influence the persistent surface and hard X-ray signals substantially.

Thus, the picture we envisage is that the anti-glitch creates plasma loading with a stronger twist in polar zones that allows some transient pair production and radio emission once the wind density drops and the outflow becomes optically thin. Then later in the wind abatement phase, the field twist relaxes back to its persistent twist configuration. This conjecture motivates deeper study of field morphology and its evolution via Ohmic dissipation in concert with gamma-ray opacity and pair-creation considerations. On the observational side, NASA's (the National Aeronautics and Space Administration's) new Imaging X-ray Polarimetry Explorer could help constrain field structure in bright magnetars around (spin-down) glitch epochs through its polarization measurements of soft X-ray emission emanating from their surfaces.

Radiation from the strong wind

A long-lived non-thermal-like radiation signal associated with the hot wind would be expected, probably spanning X-rays/extreme ultraviolet down to the optical/infrared/millimetre band as the wind adiabatically cools on its path out to R_{lc} . Its bolometric luminosity would be a small fraction of the wind luminosity, that is, $L_w \lesssim 7 \times 10^{39}$ erg s⁻¹ for $\delta t = 10$ h under the simple assumption of a pure dipole (or $L_{\rm w} \lesssim 7 \times 10^{37}$ erg s⁻¹ for a polar cap size an order of magnitude larger, see above). The intrinsic radiation efficiency is small in wind/jet systems, on the order of 0.1-1%, particularly if it is baryon loaded (that is, hydrogenic), as exemplified in supernovae and gamma-ray bursts: heat plus radiation pressure is efficiently converted into bulk kinetic energy of the plasma. The high opacity of the wind just above the stellar surface will drive it towards thermal equilibrium in all but a thin outer sheath. Using $L_{\nu} = 4\pi\sigma T^4 R^2 \lesssim 10^{38} \text{ erg s}^{-1}$ (where L_{ν} is the radiation bolometric luminosity), one quickly estimates the plasma/radiation temperature at the surface to be $T \lesssim 2 \times 10^7$ K = 1.6 keV for the δt = 10 h case, using the Stefan-Boltzmann law. As the wind flows to higher altitudes, it quickly cools according to the adiabatic expansion law where $V^{-1}T$ is constant, with $y \approx 5/3$ as the ratio of specific heats. For dipole field morphology, the comoving volume of the wind is $V \propto 1/\rho \propto R^3$, whereas for an isotropic wind above R_{eq} , $V \propto 1/\rho \propto R^2$, respectively yielding $T \propto R^{-2}$ and $T \propto R^{-4/3}$. Thus, the wind temperature drops below 10³ K by the time it reaches $R_{\rm eq} \approx 150 R_{\rm ns}$, and the 'isotropic' optical luminosity ($\propto T^4 R^2$) is 10^{25} erg s⁻¹ or much less. The small solid angle lowers the potential visibility of any radiation signal associated with the ephemeral wind.

The ensemble picture is then that if $\delta t \approx 10$ h, the radiation would not be easily observed by large-field-of-view instruments such as Fermi-GBM and Swift-BAT in X-rays nor by Zwicky Transient Facility or Panoramic Survey Telescope and Rapid Response System in the optical. Furthermore, assuming that the glitch epoch coincides with the October 4 NuSTAR observation (Fig. 7 and Supplementary Table 1), we set a 3σ upper limit on any associated X-ray flux enhancement to be about 10^{-12} erg s⁻¹, or a luminosity of about 10^{34} erg s⁻¹ at a distance 42 of 10 kpc. This is highly indicative of further enlargement of the open-field-line region or baryonic loading of the wind, both of which lower its radiative efficiency. A long-duration radio afterglow might also be expected where the wind deposits its kinetic energy in the circum-magnetar medium, somewhat analogous to that seen⁵⁴ for the giant flare of SGR 1806-20. Covering the next anti-glitch epoch with daily cadence will provide pivotal clues elucidating on the physical properties of the outflow: mass content, total energetics, radiative efficiency and so on.

Context concerning the 28 April 2020 FRB and May 24 radio bursts

The spin ephemerides for SGR 1935+2154 around the 28 April 2020 FRB are not well constrained due to sparse data coverage³, and the

1 frequency measurement hours before the 28 April 2020 FRB had a 1σ uncertainty of 2.0×10^{-6} Hz. On the other hand, the timing solution surrounding the May radio bursts¹² is based on four TOAs³. Hence, we cannot place meaningful limits on the size of a putative spin-down glitch at the time of either radio event. Interestingly, deep observations with several radio dishes⁴³ including the FAST radio telescope¹⁴ have not revealed any pulsed radio emission following these bursts. Hence, while our observational result strongly argues that a spin-down glitch is associated with, and probably facilitated, the production of FRB-like bursts and pulsed radio emission, it is unclear whether it is a universal necessity or the most stringent condition for either. For instance, the TOAs of the two May and three October radio bursts fully covered a single magnetar rotation, which argues against emission from strictly open magnetic field lines. Hence, it is possible that an outflow along quasi-polar but closed field lines may still result in the production of an FRB-like burst^{55,56} without causing a strong spin-down glitch or pulsed radio emission. Other factors could come into play, for example, the state of the magnetar. For instance, during the earlier radio bursts SGR 1935+2154 was still in outburst, emitting bright gamma-ray bursts and a pulsed hard X-ray component, both of which are not detected in October/November⁴⁴. Continued radio and high-energy monitoring of all magnetars is essential to drawing a broader picture that could connect the many transient facets that these topical sources display.

Data availability

NICER raw data (level 1) and calibrated (level 2) data files were generated at the Goddard Space Flight Center large-scale facility. These data files are publicly available and can be found at https://heasarc.gsfc.nasa.gov/FTP/nicer/data/obs/. XMM-Newton and NuSTAR data files are also publicly available from the XMM-Newton Science Archive (https://heasarc.gsfc.nasa.gov/W3Browse/xmm-newton/xmmmaster.html) and the NuSTAR Master Catalog table (https://heasarc.gsfc.nasa.gov/W3Browse/all/numaster.html). Light curve and spectral data presented in the various plots of the manuscript are available from the corresponding authors upon request.

Code availability

Reduction and analysis of the data were conducted using publicly available codes provided by HEASARC, which is a service of the Astrophysics Science Division at NASA/GSFC and the High Energy Astrophysics Division of the Smithsonian Astrophysical Observatory. For NICER and NuSTAR, we used NICERDAS version v.008c and NUSTARDAS version v.2.1.1, respectively, part of HEASOFT 6.29c (https://heasarc.gsfc.nasa.gov/docs/software/lheasoft). For XMM-Newton, we utilize the publicly available SAS version 19.1.0. Spectral analysis was conducted using Xspec version 12.12.0g (https://heasarc.gsfc.nasa.gov/docs/xanadu/xspec/). The emcee MCMC sampler is a public software available at https://emcee.readthedocs.io/en/stable/. Custom codes for the timing analysis routines are available upon reasonable request from the corresponding authors.

References

- Israel, G. L. et al. The discovery, monitoring and environment of SGR J1935+2154. Mon. Not. R. Astron. Soc. 457, 3448–3456 (2016).
- Younes, G. et al. X-ray and radio observations of the magnetar SGR J1935+2154 during its 2014, 2015, and 2016 outbursts. Astrophys. J. 847, 85 (2017).
- Younes, G. et al. NICER view of the 2020 burst storm and persistent emission of SGR 1935+2154. Astrophys. J. Lett. 904, L21 (2020).
- Petroff, E., Hessels, J. W. T. & Lorimer, D. R. Fast radio bursts. Astron. Astrophys. Rev. 27, 4 (2019).
- Bochenek, C. D. et al. A fast radio burst associated with a Galactic magnetar. Nature 587, 59–62 (2020).

- CHIME/FRB Collaboration A bright millisecond-duration radio burst from a Galactic magnetar. Nature 587, 54–58 (2020).
- Archibald, R. F. et al. An anti-glitch in a magnetar. Nature 497, 591–593 (2013).
- 8. Younes, G. et al. A radiatively quiet glitch and anti-glitch in the magnetar 1E 2259+586. Astrophys. J. Lett. **896**, L42 (2020).
- 9. Dib, R. & Kaspi, V. M. 16 yr of RXTE monitoring of five anomalous X-ray pulsars. *Astrophys. J.* **784**, 37 (2014).
- Woods, P. M. et al. Variable spin-down in the soft gamma repeater SGR 1900+14 and correlations with burst activity. Astrophys. J. Lett. 524, L55–L58 (1999).
- Good, D. & CHIME/FRB Collaboration CHIME/FRB detection of three more radio bursts from SGR 1935+2154. Astron. Telegr. 14074, 1 (2020).
- Kirsten, F. et al. Detection of two bright radio bursts from magnetar SGR 1935+2154. Nat. Astron. 5, 414–422 (2020).
- 13. Zhu, W. et al. FAST detection of radio bursts and pulsed emission from SGR J1935+2154. Astron. Telegr. **14084**, 1 (2020).
- Lin, L. et al. No pulsed radio emission during a bursting phase of a Galactic magnetar. Nature 587, 63–65 (2020).
- Parfrey, K., Beloborodov, A. M. & Hui, L. Twisting, reconnecting magnetospheres and magnetar spindown. Astrophys. J. Lett. 754, L12 (2012).
- Mastrano, A., Suvorov, A. G. & Melatos, A. Interpreting the AXP 1E 2259+586 antiglitch as a change in internal magnetization. *Mon. Not. R. Astron. Soc.* 453, 522–530 (2015).
- Thompson, C. et al. Physical mechanisms for the variable spin-down and light curve of SGR 1900+14. Astrophys. J. 543, 340–350 (2000).
- Harding, A. K., Contopoulos, I. & Kazanas, D. Magnetar spin-down. Astrophys. J. Lett. 525, L125–L128 (1999).
- Sturrock, P. A. A model of pulsars. Astrophys. J. 164, 529–556 (1971).
- Wadiasingh, Z. et al. The fast radio burst luminosity function and death line in the low-twist magnetar model. Astrophys. J. 891, 82 (2020).
- Bai, X.-N. & Spitkovsky, A. Modeling of gamma-ray pulsar light curves using the force-free magnetic field. Astrophys. J. 715, 1282–1301 (2010).
- Kalapotharakos, C., Kazanas, D., Harding, A. & Contopoulos,
 Toward a realistic pulsar magnetosphere. Astrophys. J. 749, 2 (2012).
- Harding, A. K., Tademaru, E. & Esposito, L. W. A curvatureradiation-pair-production model for gamma-ray pulsars. Astrophys. J. 225, 226–236 (1978).
- Baring, M. G. & Harding, A. K. Photon splitting and pair creation in highly magnetized pulsars. Astrophys. J. 547, 929–948 (2001).
- Baring, M. G. & Harding, A. K. Radio-quiet pulsars with ultrastrong magnetic fields. Astrophys. J. Lett. 507, L55–L58 (1998).
- Beloborodov, A. M. & Li, X. Magnetar heating. Astrophys. J. 833, 261 (2016).
- Metzger, B. D., Margalit, B. & Sironi, L. Fast radio bursts as synchrotron maser emission from decelerating relativistic blast waves. Mon. Not. R. Astron. Soc. 485, 4091–4106 (2019).
- Ruderman, M. A. & Sutherland, P. G. Theory of pulsars: polar gaps, sparks, and coherent microwave radiation. *Astrophys. J.* 196, 51–72 (1975).
- Gendreau, K. C. et al. The Neutron star Interior Composition Explorer (NICER): design and development. Proc. SPIE 9905, 99051H (2016).
- 30. Remillard, R. A. et al. An empirical background model for the NICER X-ray timing instrument. *Astron. J.* **163**, 130 (2022).
- Strüder, L. et al. The European Photon Imaging Camera on XMM-Newton: the pn-CCD camera. Astron. Astrophys. 365, L18–L26 (2001).

- Harrison, F. A. et al. The Nuclear Spectroscopic Telescope Array (NuSTAR) high-energy X-ray mission. Astrophys. J. 770, 103 (2013).
- 33. Levan, A., Kouveliotou, C. & Fruchter, A. Identification of the infrared counterpart of SGR 1935+2154 with the Hubble Space Telescope. *Astrophys. J.* **854**, 161 (2018).
- Buccheri, R. et al. Search for pulsed gamma-ray emission from radio pulsars in the COS-B data. Astron. Astrophys. 128, 245–251 (1983).
- 35. Ray, P. S. et al. Precise γ-ray timing and radio observations of 17 Fermi γ-ray pulsars. Astrophys. J. Suppl. **194**, 17 (2011).
- 36. Livingstone, M. A. et al. X-ray and radio timing of the pulsar in 3C 58. Astrophys. J. **706**, 1163–1173 (2009).
- Foreman-Mackey, D., Hogg, D. W., Lang, D. & Goodman, J. emcee: the MCMC hammer. Publ. Astron. Soc. Pac. 125, 306–312 (2013).
- 38. Archibald, R. F., Scholz, P., Kaspi, V. M., Tendulkar, S. P. & Beardmore, A. P. Two new outbursts and transient hard X-rays from 1E 1048.1-5937. *Astrophys. J.* **889**, 160 (2020).
- 39. Hu, C.-P. et al. NICER observation of the temporal and spectral evolution of Swift J1818.0-1607: a missing link between magnetars and rotation-powered pulsars. *Astrophys. J.* **902**, 1 (2020).
- 40. Woods, P. M. et al. Changes in the X-ray emission from the magnetar candidate 1E 2259+586 during its 2002 outburst. *Astrophys. J.* **605**, 378–399 (2004).
- Gavriil, F. P., Kaspi, V. M. & Woods, P. M. A comprehensive study of the X-ray bursts from the magnetar candidate 1E 2259+586. Astrophys. J. 607, 959–969 (2004).
- Zhong, S.-Q., Dai, Z.-G., Zhang, H.-M. & Deng, C.-M. On the distance of SGR 1935+2154 associated with FRB 200428 and hosted in SNR G57.2+0.8. Astrophys. J. Lett. 898, L5 (2020).
- 43. Bailes, M. et al. Multifrequency observations of SGR J1935+2154. *Mon. Not. R. Astron. Soc.* **503**, 5367–5384 (2021).
- 44. Borghese, A. et al. The first 7 months of the 2020 X-ray outburst of the magnetar SGR J1935+2154. *Mon. Not. R. Astron.* Soc. **516**, 602–616 (2022).
- 45. Blaskiewicz, M., Cordes, J. M. & Wasserman, I. A relativistic model of pulsar polarization. *Astrophys. J.* **370**, 643–669 (1991).
- Dyks, J., Rudak, B. & Harding, A. K. On the methods of determining the radio emission geometry in pulsar magnetospheres. Astrophys. J. 607, 939–948 (2004).
- 47. Daugherty, J. K. & Harding, A. K. Electromagnetic cascades in pulsars. *Astrophys. J.* **252**, 337–347 (1982).
- Hu, K., Baring, M. G., Wadiasingh, Z. & Harding, A. K. Opacities for photon splitting and pair creation in neutron star magnetospheres. *Mon. Not. R. Astron. Soc.* 486, 3327–3349 (2019).
- 49. Tchekhovskoy, A., Philippov, A. & Spitkovsky, A. Three-dimensional analytical description of magnetized winds from oblique pulsars. *Mon. Not. R. Astron.* Soc. **457**, 3384–3395 (2016).
- Thompson, C., Lyutikov, M. & Kulkarni, S. R. Electrodynamics of magnetars: implications for the persistent X-ray emission and spin-down of the soft gamma repeaters and anomalous X-ray pulsars. Astrophys. J. 574, 332–355 (2002).
- Hu, K., Baring, M. G., Harding, A. K. & Wadiasingh, Z. High-energy photon opacity in the twisted magnetospheres of magnetars. Astrophys. J. 940, 91 (2022).
- 52. Beloborodov, A. M. Untwisting magnetospheres of neutron stars. *Astrophys. J.* **703**, 1044–1060 (2009).
- Weisskopf, M. C. et al. The Imaging X-Ray Polarimetry Explorer (IXPE): pre-launch. J. Astron. Telesc. Instrum. Syst. 8, 026002 (2022).
- Gaensler, B. M. et al. An expanding radio nebula produced by a giant flare from the magnetar SGR 1806-20. *Nature* 434, 1104–1106 (2005).

- Ioka, K. Fast radio burst breakouts from magnetar burst fireballs. Astrophys. J. Lett. 904, L15 (2020).
- Younes, G. et al. Broadband X-ray burst spectroscopy of the fast-radio-burst-emitting Galactic magnetar. *Nat. Astron.* 5, 408–413 (2021).

Acknowledgements

A portion of this work was supported by NASA through the NICER mission and the Astrophysics Explorers Program. This research has made use of data and software provided by the High Energy Astrophysics Science Archive Research Center (HEASARC), which is a service of the Astrophysics Science Division at NASA/GSFC and the High Energy Astrophysics Division of the Smithsonian Astrophysical Observatory, G.Y.'s research is supported by an appointment to the NASA Postdoctoral Program at the Goddard Space Flight Center, administered by Oak Ridge Associated Universities under contract with NASA. M.G.B. acknowledges the support of the National Science Foundation through grant AST-1813649. A.B.P. is a McGill Space Institute (MSI) Fellow and a Fonds de Recherche du Quebec-Nature et Technologies (FRQNT) postdoctoral fellow. S.G. acknowledges the support of the Centre National d'Etudes Spatiales (CNES). T.E. acknowledges Hakubi projects of Kyoto University and RIKEN, and is supported by JSPS/ MEXT KAKENHI grant numbers 15H00845 and 17K18776. W.C.G.H. acknowledges support through grant 80NSSC22K0397 from NASA. A.B. is supported by a Juan de la Cierva fellowship. C.-P.H. acknowledges support from the Ministry of Science and Technology in Taiwan through grant MOST 109-2112-M-018-009-MY3. W.A.M acknowledges support from the Jet Propulsion Laboratory, California Institute of Technology, under a Research and Technology Development Grant through a contract with NASA. US government sponsorship is acknowledged. G.Y. thanks V. Kaspi and T. Strohmayer for providing constructive comments on the manuscript and P. Ray for guidance on the timing analysis.

Author contributions

G.Y. performed the data analysis and contributed to the writing of the associated text. M.G.B. led the interpretative elements and was responsible for the writing of the associated text. A.K.H., T.E., Z.W., W.C.G.H., S.G., A.B., A.B.P., T.G., A.J.v.d.H., C.-P.H., E.G., G.K.J., C.K., L.L. and W.A.M. contributed to the discussion and editing of the manuscript. A.B.P. and G.Y. were responsible for acquiring the majority of the NICER data through the Director's Discretionary Time. E.G. and L.L. were responsible for acquiring part of the XMM-Newton and NuSTAR data. A.B. was responsible for acquiring the XMM-Newton October 1 data and part of the NICER data. K.G. is the NICER principal investigator; he approved the Director's Discretionary Time observations. Z.A. is the NICER project scientist and deputy principal investigator; he contributed to the scheduling of the NICER observations.

Competing interests

The authors declare no competing interests.

Additional information

Supplementary information The online version contains supplementary material available at https://doi.org/10.1038/s41550-022-01865-y.

Correspondence and requests for materials should be addressed to G. Younes or M. G. Baring.

Peer review information *Nature Astronomy* thanks Shriharsh Tendulkar and the other, anonymous, reviewer(s) for their contribution to the peer review of this work.

Reprints and permissions information is available at www.nature.com/reprints.

Publisher's note Springer Nature remains neutral with regard to jurisdictional claims in published maps and institutional affiliations.

Springer Nature or its licensor (e.g. a society or other partner) holds exclusive rights to this article under a publishing agreement with the author(s) or other rightsholder(s); author self-archiving of the accepted manuscript version of this article is solely governed by the terms of such publishing agreement and applicable law.

© The Author(s), under exclusive licence to Springer Nature Limited 2023

¹Astrophysics Science Division, NASA/GSFC, Greenbelt, MD, USA. ²Department of Physics, The George Washington University, Washington DC, USA. ³Department of Physics and Astronomy, Rice University, Houston, TX, USA. ⁴Theoretical Division, Los Alamos National Laboratory, Los Alamos, NM, USA. ⁵Extreme Natural Phenomena RIKEN Hakubi Research Team, Cluster for Pioneering Research, RIKEN, Wako, Japan. ⁶Department of Astronomy, University of Maryland, College Park, MD, USA. ⁷Center for Research and Exploration in Space Science and Technology, NASA/GSFC, Greenbelt, MD, USA. ⁸Department of Physics, McGill University, Montréal, Quebec, Canada. ⁹McGill Space Institute, McGill University, Montréal, Quebec, Canada. ¹⁰Division of Physics, Mathematics, and Astronomy, California Institute of Technology, Pasadena, CA, USA. ¹¹Department of Physics and Astronomy, Haverford College, Haverford, PA, USA. ¹²IRAP, CNRS, Toulouse, France. ¹³Université de Toulouse, CNES, UPS-OMP, Toulouse, France. ¹⁴Institute of Space Sciences (ICE, CSIC), Barcelona, Spain. ¹⁵Institut d'Estudis Espacials de Catalunya (IEEC), Barcelona, Spain. ¹⁶Sabancı University, Faculty of Engineering and Natural Sciences, Istanbul, Turkey. ¹⁷Istanbul University, Science Faculty, Department of Astronomy and Space Sciences, Istanbul, Turkey. ¹⁸Department of Physics, National Changhua University of Education, Changhua, Taiwan. ¹⁹National Space Institute, Technical University of Denmark, Lyngby, Denmark. ²⁰Department of Astronomy, Beijing Normal University, Beijing, P. R. China. ²¹Jet Propulsion Laboratory, California Institute of Technology, Pasadena, CA, USA. ¹²Pe-mail: george.a.younes@nasa.gov; baring@rice.edu